

Radio emission during the formation of stellar clusters in M33

Edvige Corbelli¹, Jonathan Braine², and Fatemeh S. Tabatabaei^{3,4,5}

¹ INAF-Osservatorio Astrofisico di Arcetri, Largo E. Fermi, 5, 50125 Firenze, Italy
e-mail: edvige@arcetri.astro.it

² Laboratoire d'Astrophysique de Bordeaux, Univ. Bordeaux, CNRS, B18N, allée Geoffroy Saint-Hilaire, 33615 Pessac, France

³ School of Astronomy, Institute for Research in Fundamental Sciences, P.O. Box 19395-5531, Tehran, Iran

⁴ Instituto de Astrofísica de Canarias, 38205 San Cristbal de La Laguna, Tenerife, Spain

⁵ Max-Planck-Institut für Astronomie, Königstuhl 17, 69117 Heidelberg, Germany

Received; accepted

ABSTRACT

Context.

Aims. We investigate thermal and non-thermal radio emission associated with the early formation and evolution phases of Young Stellar Clusters (YSCs) selected by their MIR emission at $24 \mu\text{m}$ in M33. We consider regions in their early formation period, compact and totally embedded in the molecular cloud, and in the more evolved and exposed phase.

Methods. Thanks to recent radio continuum surveys between 1.4 and 6.3 GHz we are able to find radio source counterparts to more than 300 star forming regions of M33. We identify the thermal free-free component for YSCs and their associated molecular complexes using the $\text{H}\alpha$ line emission.

Results. A cross-correlation of MIR and radio continuum is established from bright to very faint sources, with the MIR-to-radio emission ratio that shows a slow radial decline throughout the M33 disk. We proof the nature of candidate embedded sources by recovering the associated faint radio continuum luminosities. By selecting exposed YSCs with reliable $\text{H}\alpha$ flux, we establish and discuss the tight relation between $\text{H}\alpha$ and the total radio continuum at 5 GHz over 4 orders of magnitude. This holds for individual YSCs as well as for the molecular clouds hosting YSCs and allowed us to calibrate the radio continuum - star formation rate relation at small scales. On average about half of radio emission at 5 GHz in YSCs is non-thermal with a large scatter. For exposed but compact YSCs and their molecular clouds the non-thermal radio continuum fraction increases with source brightness, while for large HII regions the non-thermal fraction is lower and shows no clear trend. This has been found for YSCs with and without identified SNRs and underlines the possible role of massive stars in triggering particle acceleration through winds and shocks: these particles diffuse throughout the native molecular cloud prior to cloud dispersal.

Key words. Galaxies: individual (M 33) – Galaxies: ISM, star formation, star clusters – ISM: cosmic rays, molecules, dust, magnetic fields – Radio continuum: ISM

1. Introduction

The radio continuum-infrared (hereafter IR) correlation in galaxies has been investigated since the data release by IRAS mission (e.g. Helou et al. 1985; Bell 2003). In the past 35 years a lot of effort has been spent to investigate the frequency ranges in the IR and radio continuum for which the correlation is the tightest and how this depends on spatial scale. In the IR domain the focus has been to distinguish warm dust emitting in the mid-infrared (MIR) and heated by star formation, from cold dust heated by the interstellar radiation field (ISRF) and emitting in the far-infrared (FIR). In the radio continuum both thermal (free-free) and non-thermal (synchrotron) emission are linked to the formation of stars since this process is responsible for the free electrons, as well as for turbulent magnetic field amplification and cosmic ray (hereafter CR) production (e.g. Schleicher & Beck 2013; Schober et al. 2016; Tabatabaei et al. 2013b). A key question is the spatial scale involved in the dust-to-radio correlation and to this purpose nearby galaxies such as LMC, M33, M51 etc.. have been analyzed by using wavelet decomposition and maps at several spatial resolutions, from 50 pc out to the kpc scale, for

the radio and IR emission (Hughes et al. 2006; Tabatabaei et al. 2007a; Dumas et al. 2011; Tabatabaei et al. 2013a). On large scales the ordered magnetic field seems to play a major role in driving non-thermal emission, especially where cosmic rays are able to diffuse away from star forming sites before losing their energy. Thus the magnetic field might be coupled to cold dust by density enhancement in the diffuse ISM (Basu et al. 2017). In M51 Dumas et al. (2011) explored how the relation between the MIR and radio continuum depends on the local environment such as spiral arms, interarm regions, outer versus inner disk and found that a linear relation holds only along the spiral arms with radio synchrotron emission being suppressed in the central regions.

On small scales it is interesting to study the non-thermal and thermal component and how these relates to the warm dust as a function of the ISM properties and environment in the galactic disk. Data in the radio continuum at 1.4 GHz and at $60 \mu\text{m}$ for the LMC at spatial resolution between 50 pc and 1.5 kpc has been analyzed by Hughes et al. (2006). They found that on small scales the thermal radio emission correlates better with

the warm dust component while the non-thermal FIR correlation breaks down below a certain scale possibly because of the large diffusion length of cosmic rays. More recently, a work on IC10 by Basu et al. (2017) underlines that also at smaller scales, between 50 and 200 pc, the non-thermal radio emission establishes a better correlation with the dust emission at $70 \mu\text{m}$ than with the warm dust at $24 \mu\text{m}$. However there are no studies analyzing individual star forming regions, where the $24 \mu\text{m}$ emission peaks.

The large scale magnetic field in M33 exhibit a spiral structure with a decrease in the radio thermal fraction going radially outwards (Tabatabaei et al. 2007c). At kpc scales in M33 the warm dust-thermal radio correlation is stronger than the cold dust-non thermal radio correlation (Tabatabaei et al. 2007a), although a cold dust non-thermal correlation still holds. Analysis of the radio emission in the closest spiral galaxies (Tabatabaei et al. 2013a) has show that the non thermal-IR correlation is weaker in M33 than in M31 on large scales, but it is stronger than in M 31 on scales <1 kpc. This has been explained by the smaller propagation length of CR electrons in M33, due to its turbulent magnetic field structure. At smaller scales the turbulent magnetic field might become more important as turbulent gas motion injects energy into the ISM (Tabatabaei et al. 2008). If this is a general property of the M33's ISM, the non thermal-IR correlation should also hold on scales where the turbulent magnetic field is strongest, i.e., in the star forming clouds.

For nearby galaxies the sensitivity and spatial resolution of infrared and radio surveys is now sufficiently high that it is possible to isolate individual star forming regions with stellar masses as low as a few hundreds solar masses (Sharma et al. 2011; White et al. 2019). This means that instead of focusing on the spatial scale and on a pixel by pixel analysis one can examine the radio and IR emission in individual star forming regions and how this depends on characteristic properties of the young cluster such as mass and age and more in general on the energy input that massive stars can provide. In this paper we analyze the radio continuum and MIR emission in individual star forming sites of M33, the closest blue spiral galaxy. This will allow us to test whether the correlation between the non-thermal radio emission and the MIR emission found down to 200 pc scale (Tabatabaei et al. 2013a) holds also at smaller scales between the emission of individual young stellar clusters. Previous works have presented a catalogue of infrared selected star forming regions across the whole disk of M33 (Sharma et al. 2011) which has been complemented by a catalogue of GMCs (Corbelli et al. 2017) and recently a list of radio-continuum sources in the M33 area became available (White et al. 2019), some of which might be related to the M33 disk. The spatial resolution at $24 \mu\text{m}$ is comparable to that of the recent radio-continuum surveys. Our aim is to investigate the correlations between the radio continuum and other star formation tracers such as $H\alpha$ or MIR emission and investigate the dominant mechanism that provides radio emission, if thermal or non thermal, across a variety of star forming regions. While it is clear that the turbulent magnetic field is enhanced in star forming regions it is less clear how this depends on the characteristic of the region and its location in the disk. Furthermore the creation and propagation of CRs might depend on the galaxy (Tabatabaei et al. 2013a) and on characteristics of the SF region.

Currently most of the models involving CRs acceleration are based on supernova (SN) explosions and their remnants (SNRs). In particular these models can explain the CR production rate, the composition and anisotropy in our Galaxy. However, the steepness and the presence of breaks in SN spectra as well as the difficulties in explaining the very energetic CRs opens the pos-

sibility to other types of acceleration mechanisms. Moreover the duration of the SN shock might be too short to explain the propagation away from the remnants that is needed to explain some observation. Over the last decade, space- and ground-based telescopes have revealed many classes of Galactic γ -ray sources, such as clusters of young stars, which might be associated to CR accelerators. As underlined recently by Aharonian et al. (2019) the acceleration could take place in the vicinity of the stars or in superbubbles, caused by interacting winds of massive stars as those in OB associations. A fraction of stellar wind mechanical energy may be transferred to relativistic CRs by diffuse shock acceleration at the wind boundary (Cesarsky & Montmerle 1983; Parizot et al. 2004; Padovani et al. 2019). These will spiral around the fluctuating amplified magnetic fields of the star forming region emitting non-thermal radio waves. To test these possibilities recently identified SNRs in star forming regions of M33 (White et al. 2019) can be used for assessing their role in enhancing the non thermal radio emission in SF regions .

The plan of the paper is the following: In Section 2 we present the data and the method to establish the association between MIR and radio sources. In Section 3 we present the correlation between radio continuum and MIR fluxes in exposed YSCs and in the embedded star forming sites in M33. In Section 4 we derive the non-thermal fractions and the relative implications. In Section 5 we present some preliminary results on radio emission from molecular clouds, and in Section 6 we discuss the link between the star formation and radio emission. Section 7 summarizes the main results of our analysis.

2. The YSC sample and multiwavelength data

In this Section we describe how we select candidate YSCs of M33 during their formation and early evolutionary phases and how we retrieve the emission at other wavelengths. We use three catalogues now available for M33: a $24 \mu\text{m}$ source catalogue (Sharma et al. 2011), a giant molecular cloud (GMC) catalogue (Corbelli et al. 2017) and a radio continuum source catalogue (White et al. 2019). The association is done by matching the positions in the sky of the objects in these catalogues because the shape and extend of the emission of a star forming region in the MIR and in the radio continuum might not be the same. The hot dust for example might be located closer to the GMC center or to the shell of an expanding ionized bubble while non-thermal radio continuum emission might peak close to a SNR.

2.1. The MIR source catalogue

Dust emission at MIR wavelengths has been investigated through data of the Multiband Imaging Photometer (MIPS) on board *Spitzer* processed as described by Verley et al. (2007). Corbelli et al. (2017) selected 630 MIR sources from the list of Sharma et al. (2011) that are candidate YSCs in the early formation and evolutionary phases: the results of the classification, together with the most relevant parameters of the GMCs and YSCs, can be found in their online tables. The YSCs were sorted into classes based on their emission in the MIR, FUV, and $H\alpha$ bands and according to the association with GMCs. The classification helps in drawing a possible evolutionary sequence and the relative timescales see (Corbelli et al. 2017) for more details. We recall the classification scheme of the MIR sources and the number of MIR sources in each category:

- class b: 97 MIR sources, associated with GMCs, with no optical counterpart (with no or very weak $H\alpha$ peak)

- class c: 410 YSCs with optical counterpart
 - c1: 55 YSCs associated with GMCs with coincident $H\alpha$ and MIR emission peaks but FUV emission spatially shifted or absent
 - c2: 218 YSCs associated with GMCs with coincident $H\alpha$, FUV and MIR emission peaks
 - c3: 139 YSCs not associated with GMCs but with optical and FUV counterparts; these often have weak $H\alpha$ emission
- class d: 19 MIR sources associated with GMCs which are ambiguous for b or c1/c2 class
- class e: 104 MIR sources not associated with GMCs and with no $H\alpha$ emission, some FUV may be present

The b-c1-c2-d-type are sources associated with giant molecular clouds (GMCs). The b-type are called embedded because there is no FUV or $H\alpha$ counterparts, while c-type are exposed star forming regions with FUV and $H\alpha$ counterpart and some of them (c1 and c2) are associated with GMC while others (c3) are not. The d-type are ambiguous between b-and c-type. From now on we shall refer to the c-class as exposed YSCs and to the b-type as embedded YSCs. Extinction is high for b-type sources with weak or no UV/optical counterpart, which likely represent the early phases of SF. The c1-type YSCs have visible $H\alpha$ but not FUV emission and show on average higher extinction than the c2-type YSCs, where FUV emission is also detected. The c1-type YSCs may represent YSCs at an earlier stage than c2-type YSCs, even though the YSC age determination is not precise enough to separate these two classes. The most luminous MIR sources are of c2-type and are clusters that have very likely completed the formation process. This is also the largest class of MIR sources for which the coincident peaks in the UV and $H\alpha$ bands enabled more precise estimates of the age and mass of the associated YSC.

The e-type sources have only MIR emission but unlike the b-type these do not have any associated GMC. We marginally consider the e-type in this paper. As shown in subsequent Sections and also in the paper by Corbelli et al. (2019) where deep CO searches have been carried out, the e-type are highly contaminated by background sources and thus most of them do not belong to M33. Background contamination is particularly relevant for dim sources, with flux at $24\mu\text{m}$ smaller than 5 mJy, and no associated molecular cloud or $H\alpha$ emission such as type-e sources Corbelli et al. (2019). We cannot exclude, however that a few of them might be embedded YSCs in low mass molecular clouds.

2.2. The molecular cloud catalogue

Using the IRAM 30m CO J=2-1 data cube of M33, we identified 566 GMCs, as described in Corbelli et al. (2017), and whose properties are listed in the GMCs catalogue. The GMC masses are between 2×10^4 and $2\times 10^6 M_{\odot}$ and GMC radii between 10 and 100 pc. The number of GMCs above the survey completeness limit ($M_{H_2} \geq 6.3 \times 10^4 M_{\odot}$) is 490. Corbelli et al. (2017) classified the GMCs as non-starforming (class A), with embedded SF (B), or with exposed SF (C). A few ambiguous cases are in class D. The FUV, $H\alpha$ and MIR emission maps of M33 have been used to classify the GMCs.

The majority of the MIR sources in the inner zones ($R < 4$ kpc) lie within a GMC boundary while this is not true for MIR sources in the outer disk. There is an extraordinary spatial correspondence between the GMCs and the distribution of atomic hydrogen overdensities in the inner zones. In the outer zone there are fewer GMCs, possibly because of a steepening

of the molecular cloud mass spectrum, with a larger fraction of clouds being below the survey completeness limit.

2.3. The radio source catalogue

Recently using JVLA radio continuum maps of M33 at 1.4 and 5 GHz at a spatial resolution of about 6 arcsec, White et al. (2019) catalogued 2875 sources with fluxes between 2 and $33000 \mu\text{Jy}$ (except for one with a flux of about 0.17 Jy) with a completeness limit around $300 \mu\text{Jy}$. Most of the luminous radio sources are stellar-like objects, background QSOs or MW stars; a few are sources associated with the two most prominent HII regions of M33, NGC 604 and NGC 595, which we exclude from the current analysis because of their extended and complex structure. White et al. (2019) have also identified SNR using the optical catalogues of Long et al. (2010); Lee & Lee (2014). Background contamination is present at all flux densities in radio but the number of background sources dominates over local sources in number as the flux gets below $300 \mu\text{Jy}$. To identify M33 sources it is therefore mandatory to use identification of other counterparts with line emission such as $H\alpha$ and molecular clouds.

2.4. Emission at other wavelengths

For MIR sources we have recovered the emission at other wavelengths, such as $H\alpha$, by aperture photometry which has been described in detail by Sharma et al. (2011). We noticed that the for radio sources coincident with MIR sources the $H\alpha$ emission in White et al. (2019) catalogue was much lower than that associated to MIR sources by Sharma et al. (2011), especially for bright sources. Accurate $H\alpha$ photometry is needed to estimate the thermal fraction of radio emission from YSCs. Therefore to trace the ionized gas associated to radio sources we perform new aperture photometry, centering a circular aperture on radio source coordinates. We set the aperture radius equal to 1.5 times the mean between the semiminor and semimajor source axis, and subtracting the local background (see Sharma et al. 2011, for more details on aperture photometry). As described by Hoopes & Walterbos (2000) M33 has, in fact, a non negligible diffuse fraction of ionized gas due to leakage of ionizing photons from HII regions and to massive stars in the field. An aperture larger than the source radius account for the position of the source center and extension which may change with wavelength. We adopt the narrow-line $H\alpha$ image of M33 obtained by Greenawalt (1998) and described in detail in Hoopes & Walterbos (2000). As suggested by the authors a 5% contamination by NII has been considered and accounted for.

Additional radio observations of M33 were carried out with the Karl Jansky Very Large Array (JVLA) 3 at C-band (5.5-7.5 GHz) in D configuration as part of the Cloud-scale Radio Survey of Star Formation and Feedback In Triangulum galaxy (CRASSFIT, Tabatabaei et al. in prep.) between November 2011 and March 2012. Two continuous base-bands (of 1024 MHz) were tuned at 5.5-6.5 GHz and 6.5-7.5 GHz, each with 8 sub-bands of 128 MHz. A mosaic of 5x5 was used to cover the inner $18' \times 18'$ star forming region including the main spiral arms with similar sensitivity. The total on-source observing time per pointing was about one hour leading to an rms noise of $6 \mu\text{J}$ per $9''.35$ beam in the final image. The two sources 3C 48 and 3C 138 were used as the primary flux density and the antenna gain phase calibrator during the observations. The data were reduced in the Orbit package (Cotton, 2008, PASP, 120, 439) using the standard VLA

calibration procedure. Each pointing was imaged and then combined into a mosaic using the wideband Orbit imager MFImage (Cotton et al. 2018, ApJ, 856, 67). We shall refer to this dataset as the 6.3 GHz map. The negative sidelobes sometime visible in the White et al. maps are not present in the 6.3 GHz map which can be used for deeper and more sensitive searches of YSCs radio counterparts.

In performing aperture photometry for radio sources on the 6.3 GHz map we use circular apertures with aperture radius equal to the source radius at 1.4 GHz convolved with the beam of the 6.3 GHz map. We subtract the local background, having corrected the 6.3 GHz map for missing short spacing, using the 'mode' function in a 3 pixel wide annulus at a distance of at least 4 pixels from source aperture boundary.

We would like to underline here that we have also performed aperture photometry without background subtraction both on $H\alpha$ and on radio continuum maps. The results discussed in the next Sections remain unchanged since flux variations are marginal with the largest flux increase being that relative to the 6.3 GHz data. In Section 4, where we separate the thermal and non-thermal radio flux at 5 GHz using $H\alpha$ emission, we also show results for a varying aperture size and using a smoothed version of the $H\alpha$ image. This has been obtained by convolving the original map (at about 3 arcsec spatial resolution) with a gaussian function of 6 arcsec FWHM, which is the spatial resolution of the 24 μm and 5 GHz maps.

Photometry for emission within GMCs is carried out using the the irregular GMC shape recovered by Corbelli et al. (2017). The shapes and GMC images are available for a subsample of them in the on-line version of Gratier et al. (2012). No background is subtracted in this case although some low level of diffuse emission might be associated with the atomic gas in the M33 disk along the line of sight to the GMC.

2.5. Uncertainties

The 1.4 GHz map of White et al. (2019) is less affected by sidelobes than the 5 GHz map and we trust the sources identified in the catalogue at 1.4 GHz. The source flux at 5 GHz can be recovered using the catalogued spectral indexes and flux at 1.4 GHz. This is in good agreement with the flux recovered at 6.3 GHz if we use the 6.3 GHz map before corrections for short spacing are applied. As noticed by White et al. (2019), source fluxes at 1.4 GHz are lower than those of Gordon et al. (1999) and to get an agreement a positive correction is needed. Increasing the 1.4 GHz fluxes of White et al. (2019) by about 30% brings them in agreement with the fluxes recovered using the 1.4 GHz map of Tabatabaei et al. (2007c) and the unpublished JVLA map at the same frequency (Tabatabaei et al. in preparation). Moreover, in the radio catalogue the HII region spectral indices are mostly positive, with a mean value of about 0.1, while we expect them to be negative because optically thick radio emission on the scale of tens of parsecs is unlikely. Increasing the 1.4 GHz fluxes by 30% implies spectral indices lower by about 0.2 and hence more physically reasonable. However, in this paper we use the 1.4 GHz data without applying any correction but we shall focus more on the high frequency emission at 5 and 6.3 GHz, for which no calibration corrections are needed. We use the White et al. (2019) data considering 30% calibration errors in addition to photometric and spectral index uncertainties.

Photometric errors for $H\alpha$ are negligible and calibration errors are of order 5%.

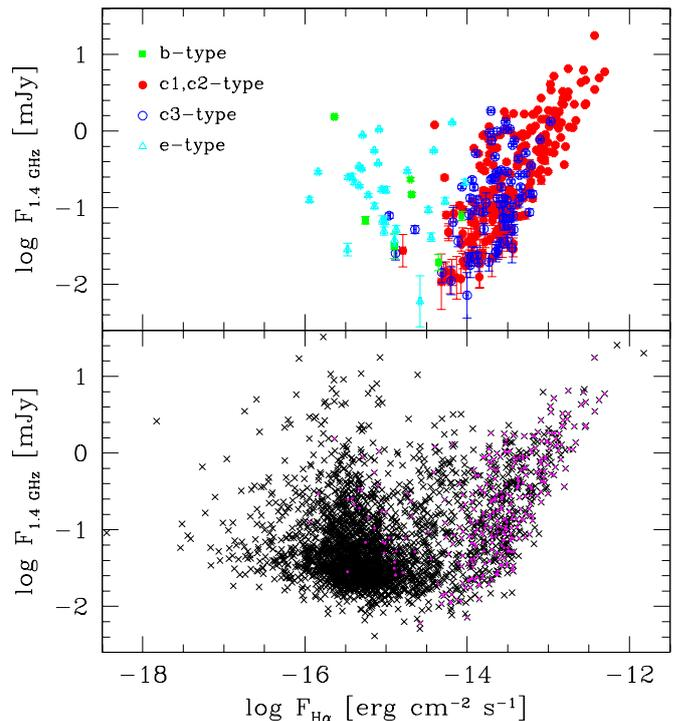


Fig. 1. The bottom panel shows the radio flux at 1.4 GHz of sources in the White et al. catalogue versus the associated $H\alpha$ flux in the same catalogue. The magenta color highlights sources in the radio catalogue which are associated with MIR sources in the catalogue of Sharma et al. (2011). These are plotted also in the upper panel where filled (green and red) and open (blue and cyan) symbols are used for MIR sources associated and not-associated with known GMCs respectively. The color coding, as indicated in the upper left corner, outlines the classification scheme of Corbelli et al. (2017) (see text for details), with blue and red colors marking MIR sources with a clear counterparts in $H\alpha$ (c-type).

3. Radio counterparts to MIR sources

To have an overview of the radio sources in the M33 area we plot in Figure 1 the radio flux at 1.4 GHz for all radio-sources in the White et al. (2019) catalogue versus $H\alpha$ emission given in the same catalogue. There are clearly two distinct source populations, one for which the radio and $H\alpha$ flux establish a correlation and the other, more numerous and with lower $H\alpha$ fluxes, for which the correlation is lost. Because of noise and diffuse emission $H\alpha$ fluxes below 10^{-15} $\text{erg s}^{-1} \text{cm}^{-2}$ are not peaks in the map. At the distance of M33 (840 kpc) this implies that we can only measure luminosities above 10^{35} erg s^{-1} equivalent to a source as faint as a B1-type star. The value of 10^{-15} $\text{erg s}^{-1} \text{cm}^{-2}$ is also the $3\text{-}\sigma$ limit for $H\alpha$ reliable counterparts of MIR selected sources using the $H\alpha$ image we adopt (Greenawalt 1998). Only in less crowded regions far from the center, where the diffuse $H\alpha$ emission is low, it is sometime possible to detect $H\alpha$ counterpart fainter than 10^{-15} $\text{erg s}^{-1} \text{cm}^{-2}$.

We identify sources in the MIR catalogue with sources in the radio catalogue. For a source at $24\ \mu\text{m}$ to be identified as the MIR counterpart of a source in the radio catalogue we require that the distance between the two sources to be less than the smaller source radius between that given at radio frequencies and that measured at $24\ \mu\text{m}$. We also visually analyzed all sources which partially overlap when their distance is less than the largest radius between the radio and MIR one, but not less than the smallest of the two, and include some of them in the list of MIR-radio associations. Not all the MIR sources that are left without a radio counterpart represent star forming sites with no radio emission because of the following:

- i) MIR background contamination on source selection
- ii) MIR source blending and problem with source centroid
- iii) shift between location of radio emission and that of hot dust
- iv) sources lying outside radio maps
- v) failure of radio source extraction because of faint radio emission contaminated by negative sidelobes.

We have a radio source counterpart for 330 of the 630 MIR sources and these are plotted in magenta color in the bottom panel of Figure 1. In the upper panel we use different colors to mark b-type, c-type and e-type MIR sources associated with radio sources in the catalogue. We find 7 out of 97 b-type sources, 287 out of 410 c-type sources, and 30 out of 104 e-type sources with counterpart in the radio catalogue. As shown in the upper panel of Figure 1 the star forming regions which have some optical or FUV counterpart (of c-type), show a clear correlation between $H\alpha$ and radio continuum flux. The red filled circles are for MIR sources associated with known GMCs in Corbelli et al. (2017) while open symbols are for MIR sources without an associated GMC because the native cloud is too faint to be detected, either because of its small mass or because the GMC is dissolving as the source evolves.

MIR sources without an optical counterpart do not follow a clear correlation with the radio counterpart but we have to underline that b- and e-type sources of low $24\ \mu\text{m}$ flux (below 5 mJy) suffer of strong background contamination. Therefore some of the MIR-sources of b- and especially of e-type with associated radio emission can be background objects (Corbelli et al. 2019). The e-type MIR sources have radio spectral indexes much more negative than YSCs, and distributed around the value of -0.8 ; this confirms that they are a different population, likely associated to background galaxies. Some MIR sources, which are not in the Figure, because don't have an associated radio source, might have suffered a displacement of the MIR emission with respect to radio peaks. This can happen for example as the HII region expands: the dust can be located just on a side of the ionized bubble while radio emission might peak where non-thermal or thermal emission is strongest. On the other hand radio emission due to embedded compact HII regions might also have been diluted in the beam.

In the bottom and middle panel of Figure 2 we plot the MIR flux at $24\ \mu\text{m}$ versus the radio continuum at 1.4 and 5 GHz respectively for all matched catalogued sources, color coded according to their class. The 5 GHz flux has been recovered using the 1.4 GHz flux and spectral indexes of White et al. (2019). There is a well defined correlation between radio and MIR emission in star forming regions. The correlation gets tighter if we consider sources at $R < 3\ \text{kpc}$ or young sources i.e. located in GMCs (red and green symbols). In the middle panel the continuous line is the best fit to the distribution which minimizes the geometrical distances to the line i.e. the sum of the squares of the distances from the data to the line. The slope of the corre-

lation shown is 0.72 and is unchanged if we replace the 5 GHz with the 6.3 GHz flux. The slope is slightly higher, 0.81, if only exposed sources hosted by molecular clouds (red dots) are considered. We would like to underline here that of the 285 HII regions identified by White et al. (2019) only 58 are coincident with MIR sources considered here. We have in our MIR sample only 31 SNRs (identified with code 11 or 9) of the total 104 SNRs with radio continuum peaks.

Radio continuum and mid-infrared radiation are both linked to the formation of massive stars and a nearly linear correlation is expected when integrated over the whole galaxy extent. The UV radiation from massive stars is partially absorbed by dust and ionizes the surrounding ISM where thermal electrons give rise to free-free emission, while shocks from winds and SNR produce cosmic rays that emit non-thermal (synchrotron) radiation. However variations in dust abundance and magnetic field strength justify possible deviations from a linear relation. Integrated over the whole galaxy the average ratio between the $24\ \mu\text{m}$ and the radio flux density at 1.4 GHz is lower than what we find in most star forming regions of M33 (Huynh et al. 2010; Appleton et al. 2004). Only regions hosting a SNR show ratios similar to galaxy integrated values. This can be attributed to the non continuous production of cosmic rays which diffuse away from star formation sites, but also to the nature of $24\ \mu\text{m}$ emission which is more enhanced where massive stars form and less diffuse than other infrared tracers. However, in M33 dust opacity in star forming regions is not high enough to absorb most of UV and optical starlight (Verley et al. 2009) and $24\ \mu\text{m}$ radiation alone does not trace star formation accurately. The dust abundance, like gas phase metal abundances (Magrini et al. 2010), decreases with galactocentric distance and this variation is also driving the sublinear relation between the $24\ \mu\text{m}$ emission and radio continuum. The lack of strong spiral arms in the regions beyond corotation (Corbelli et al. 2019) favors the birth of small star forming sites with a lower MIR-to-radio emission ratio than sites in the inner regions, closer to what is found for galaxies on a larger scale. The open blue circles at the faint end of the distribution in Figure 2, are examples of this type of YSCs. They lie mostly in the outer disk where CO lines are weaker and have no identified giant molecular clouds.

3.1. Radio continuum photometry of undetected counterparts

We now consider all the MIR sources which are associated with a GMC or that have an optical counterpart and very likely are star forming regions in the M33 disk (we refer to these as Young Stellar Clusters, hereafter YSCs). Those are listed as sources type-b,-c,-d in the classification scheme of Corbelli et al. (2017) (see their Table 2) and are in total 526, 300 of which have an associated radio source. To complement the existing radio-catalogue by deeper searches for diffuse radio-emission associated with the remaining MIR sources, we carried out aperture photometry on the radio map at 6.3 GHz. This covers a smaller region than the 5 and 1.4 GHz maps and hence a substantial fraction (about 30% of the total) of the MIR sample lies outside this map.

Of the sources inside the map which had no radio counterpart in the catalogue we detect 90% of them using aperture photometry. By adding the number of detected MIR sources with aperture photometry to the number of matched sources listed in catalogues we have a radio counterpart for 440 MIR sources. Inside the 6.3 GHz map we can claim a detection rate of 95% including catalogued and non-catalogued radio counterparts. Given

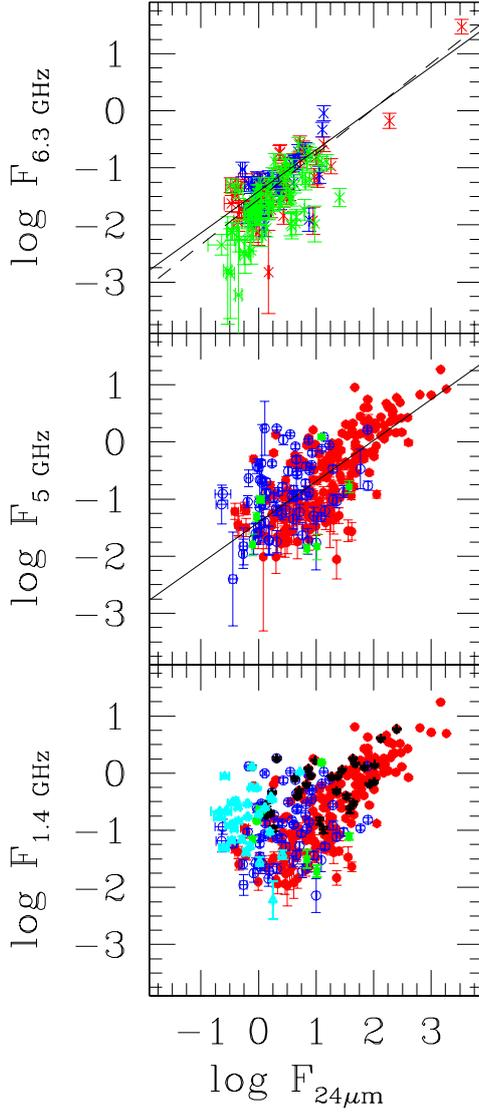


Fig. 2. The bottom panel shows the radio flux at 1.4 GHz of sources in the White et al. catalogue versus the flux at $24 \mu\text{m}$ of the associated MIR sources, color coded as in Figure 1. Flux units are mJy. The star symbols indicate the presence of identified SNR in the region (code > 8). In the middle panel the radio flux at 5 GHz has been computed using the spectral index of each radio source in the catalogue. We show only data for b- and c-type sources with the continuum line that is the best fit to them. In the upper panel we display the radio flux at 6.3 GHz from aperture photometry of b- and c-type MIR sources with no catalogued radio counterpart but covered by the 6.3 GHz survey. Color coding is the same as in the other panels although cross symbols are used for these sources. The continuum line is the same as in the middle panel while dashed line is the fit to all data in the middle and upper panel.

the fact that the non-detected sources are small and affected by beam dilution, and moreover some might have had a bright radio source nearby that artificially affected the estimated background, we can say that MIR-source located in the inner disk (at $R < 4$ kpc) and related to star-forming regions have associ-

ated radio-emission. The fraction of MIR sources with a radio counterpart at larger radii is $> 60\%$ but we cannot constrain this number better due to the limited coverage of the 6.3 GHz map.

In the upper panel of Figure 2 we show the radio flux recovered by aperture photometry on the 6.3 GHz map, versus the $24 \mu\text{m}$ flux of MIR star forming sources with no catalogued radio counterpart. The dashed line is the fit to all sources in the middle and upper panel of the Figure. Its slope is 0.80 slightly higher than the fit relative to matched catalogued sources only. Clearly YSCs without a catalogued radio counterpart have weaker radio fluxes than YSCs with similar MIR fluxes. This is also because most of these sources are still embedded, in the early phases of star formation prior to the onset of winds and shocks with enhanced turbulent magnetic fields and cosmic ray acceleration. However, there is a good agreement of the radio fluxes recovered via aperture photometry at 6.3 GHz with those recovered by source extraction at slightly lower frequency. This proves that indeed there is only a unique population of YSCs in M33 and that the relation between the radio-continuum at 6.3 GHz and the MIR flux is slightly sublinear, with the MIR flux increasing faster than the radio flux does as the YSCs becomes brighter.

4. Thermal and non-thermal radio emission

In this Section we investigate the fraction of radio emission that is linked to thermal and non-thermal processes in YSCs. To derive the thermal fraction in YSCs we use the extinction corrected $H\alpha$ flux. This has been computed using the expression of the free-free absorption coefficient in the Rayleigh-Jeans regime with the velocity averaged Gaunt factor given by Draine (2011) and assuming that hydrogen atoms provides most of the ions and free electrons:

$$\frac{k_\nu}{\text{cm}^{-1}} = 1.091 n_e n_i 10^{-25} \left(\frac{T}{10^4 \text{K}}\right)^{-1.32} \left(\frac{\nu}{1 \text{GHz}}\right)^{-2.118} \quad (1)$$

where ν is the frequency in GHz, T is the electron temperature in K, n_e and n_i are the electron and ion densities in cm^{-3} . The brightness temperature is the product between the electron temperature and the optical depth τ_ν , the latter being the integration of k_ν along the line of sight. Using the emission measure EM in $\text{cm}^{-6} \text{pc}$ we can write the brightness temperature for free-free emission as:

$$\frac{T_b^{ff}}{\text{K}} \simeq \tau_\nu T = 3.37 \cdot 10^{-3} \left(\frac{T}{10^4 \text{K}}\right)^{-0.323} \left(\frac{\nu}{1 \text{GHz}}\right)^{-2.118} \left(\frac{EM}{\text{cm}^{-6} \text{pc}}\right) \quad (2)$$

The flux density for a source of uniform brightness is

$$S_\nu^{ff} = \frac{2\nu^2 k_B T_b^{ff}}{c^2} \Omega_s \quad (3)$$

with k_B the Boltzmann's constant, c the speed of light and Ω_s the angular source extent. Using the above expression for the brightness temperature the flux density in milliJansky is

$$\frac{S_\nu^{ff}}{\text{mJy}} = 0.1033 \left(\frac{T}{10^4 \text{K}}\right)^{-0.323} \left(\frac{\nu}{1 \text{GHz}}\right)^{-0.118} \left(\frac{EM}{\text{cm}^{-6} \text{pc}}\right) \quad (4)$$

The intensity of $H\alpha$ line emission Dong & Draine (2011) is

$$\frac{I_{H\alpha}}{\text{ergs cm}^{-2} \text{s}^{-1} \text{sr}^{-1}} = 0.87 \cdot 10^{-7} \left(\frac{T}{10^4 \text{K}}\right)^{-0.94 - 0.031 \ln(T/10^4)} \left(\frac{EM}{\text{cm}^{-6} \text{pc}}\right) \quad (5)$$

For recovering $F_{H\alpha}$, the $H\alpha$ flux over the source extent, we multiply the above expression by Ω_s . We can then write the free-free flux density in milliJansky as a function of $F_{H\alpha}$ in $\text{erg cm}^{-2} \text{s}^{-1}$ as

$$\frac{S_{\nu}^{ff}}{\text{mJy}} = 1.187 \frac{F_{H\alpha}}{10^{-12} \text{ergs cm}^{-2} \text{s}^{-1}} \left(\frac{\nu}{1\text{GHz}}\right)^{-0.118} \left(\frac{T}{10^4\text{K}}\right)^{y(T)} \quad (6)$$

where we have defined $y(T)=0.619+0.031 \ln(T/10^4)$.

From now on we shall use the $H\alpha$ flux values measured by our aperture photometry centered on radio sources which are in good agreement with those of Sharma et al. (2011) centered on MIR sources. The correlation between $H\alpha$ fluxes, from our aperture photometry measurements, and fluxes at 5 GHz for radio sources associated to YSCs are shown in Figure 3. The dashed line indicates the expected $H\alpha$ flux if the radio emission were due to free-free emission only. This has been recovered using eq.(6) for an average electron temperature of 10^4 K across the star forming disk of M33. In the left panels we have not corrected the $H\alpha$ line for internal extinction (the Galactic extinction is negligible in the direction of M33).

We use the MIR emission to correct the $H\alpha$ for internal extinction according to Kennicutt et al. (2009) as follows:

$$F_{H\alpha}^{corr} = F_{H\alpha} + 0.02\nu_{24} \frac{F_{24}}{\text{erg cm}^{-2} \text{s}^{-1}} C \quad (7)$$

$$\frac{F_{H\alpha}^{corr}}{10^{-15}} = \frac{F_{H\alpha}}{10^{-15}} + 2.5 \frac{F_{24}}{\text{mJy}} C \quad (8)$$

where the $H\alpha$ flux is in $\text{erg s}^{-1} \text{cm}^{-2}$ and the observed value is $F_{H\alpha}$. C is a correction factor which takes into account the different MIR and radio source radius. The extent of MIR sources is usually larger than the associated radio sources for large fluxes and therefore we correct the $24\mu\text{m}$ flux values given by Sharma et al. (2011) for the different source extent using the factor C equal to the ratio of the radio-to-MIR source area. In the right panel of Figure 3 we show the extinction corrected $H\alpha$ flux associated to YSCs. These corrections are especially important for MIR sources associated with GMCs since extinction corrections here are larger, although for M33 these are never extremes. In Figure 3 we add the 6.3 GHz radio and $H\alpha$ fluxes for MIR sources without radio catalogued counterpart for which the radio flux at 6.3 GHz has been recovered by aperture photometry. A comparison between the left and right panels in Figure 3 shows that extinction corrections are particularly relevant for embedded YSCs. The e-type sources, not shown in the Figure, do not follow the general correlation and this confirms that these are likely background galaxies. The Figure underlines again that small and dimmer YSCs in M33 have both radio continuum and $H\alpha$ emission, although resolution and sensitivity limits imply that often these cannot be recovered by using source extraction algorithms. The relation is in agreement with that found for brighter sources and hence we conclude that they belong to the same population.

The correlation between $H\alpha$ and radio fluxes extend over 4 orders of magnitudes. The expected thermal radio emission computed from the $H\alpha$ emission using equation (6) is shown with a dashed line also in panel (b). The radio flux associated with star forming regions is 2-2.5 times stronger on average than expected if only thermal radio emission were associated to the YSCs. We notice the unambiguous presence of non-thermal emission in MIR sources with $H\alpha$ flux greater than $2 \times 10^{-13} \text{ erg s}^{-1} \text{ cm}^{-2}$ which correspond to a luminosity of $2 \times 10^{37} \text{ erg s}^{-1}$ at the distance of M33, equivalent to a cluster populated up to O7-type

star. Indeed theoretical computations predicts that only O-type stars more massive than M^* are able to produce a wind and therefore a shock. Despite the value M^* is still debated it is close to that of O7-O6 spectral type (Vink et al. 2000; Marcolino et al. 2009; Muijres et al. 2012).

4.1. Possible dependencies of non-thermal fractions on source compactness and galactocentric distance

Below we refine our computation to investigate the variations of thermal and non-thermal fractions with the luminosity, age, and local environment of the star forming regions. The electron temperature, needed to estimate the free-free emission, can be measured in HII regions through spectroscopy of auroral lines. For M33 Magrini et al. (2010) have derived how this temperature increases with galactocentric radius. Expressing the latter in kpc the radial dependence of the electron temperature in M33 reads:

$$\frac{T_e}{\text{K}} = 410 \frac{R}{\text{kpc}} + 8600 \quad (9)$$

From now on we measure the total radio flux and the corresponding $H\alpha$ flux by performing aperture photometry both on the 5 GHz map and on the $H\alpha$ map, the latter smoothed to the resolution of the radio map. We consider only YSCs of c-type i.e. MIR sources with radio counterpart in the catalogue of White et al. (2019) which are no longer fully embedded into the native molecular cloud but have an optical or UV counterpart. We divide these YSCs into 3 categories according to their radius R_s : *small* for $3 \leq R_s < 6$ arcsec, *medium* for $6 \leq R_s < 9$ arcsec, and *large* for $9 \leq R_s < 18$ arcsec. The radius R_s is the average between source semiminor and semimajor axes at 1.4 GHz as listed in the catalogue of White et al. (2019). The non-thermal component is just the difference between the total radio flux and the thermal component, the latter being computed using equation (6) with the radially dependent electron temperature T_e . To check that the resulting non-thermal fractions do not depend much on the aperture, we vary the aperture size but use consistently the same aperture on both maps and compute both backgrounds in annuli placed at distances of 3-3.5 times the source radius.

Figure 4 shows the resulting non-thermal to total radio flux ratio as a function of the 5 GHz radio flux density $F_{5\text{GHz}}$. This is the total flux density in mJy in a circular aperture whose radius is $R_{ap}=1.5R_s$. Small, medium and large sources are displayed in the top, middle and bottom rows respectively. The histograms to the left show the number of sources in each flux bin. The central panel shows the median (filled triangles) and the mean (open circles) non-thermal fractions with their standard deviations for each flux bin. The green, blue and magenta colors indicate apertures with radii of 1, 1.5 and 2 R_s respectively. We see that there is a common trend for all apertures for both the mean and median values. We have also checked our results using photometric fluxes with no background subtraction. Large sources show no clear dependence of the non-thermal fraction with radio flux density and have lower fractions than more compact sources of the same luminosity. An increase of the mean and median non-thermal fractions as a function of radio flux density are clearly seen for medium and small source sizes. The most compact sources brighter than 0.3 mJy show the steepest rise with radio flux density. These sources do not host catalogued SNRs but have non-thermal fractions $> 50\%$ at 5 GHz. Faint radio sources in low mass YSCs have a large dispersion around the mean because of the stochastic character of the Initial Mass Function (Corbelli et al. 2009) which implies that low mass

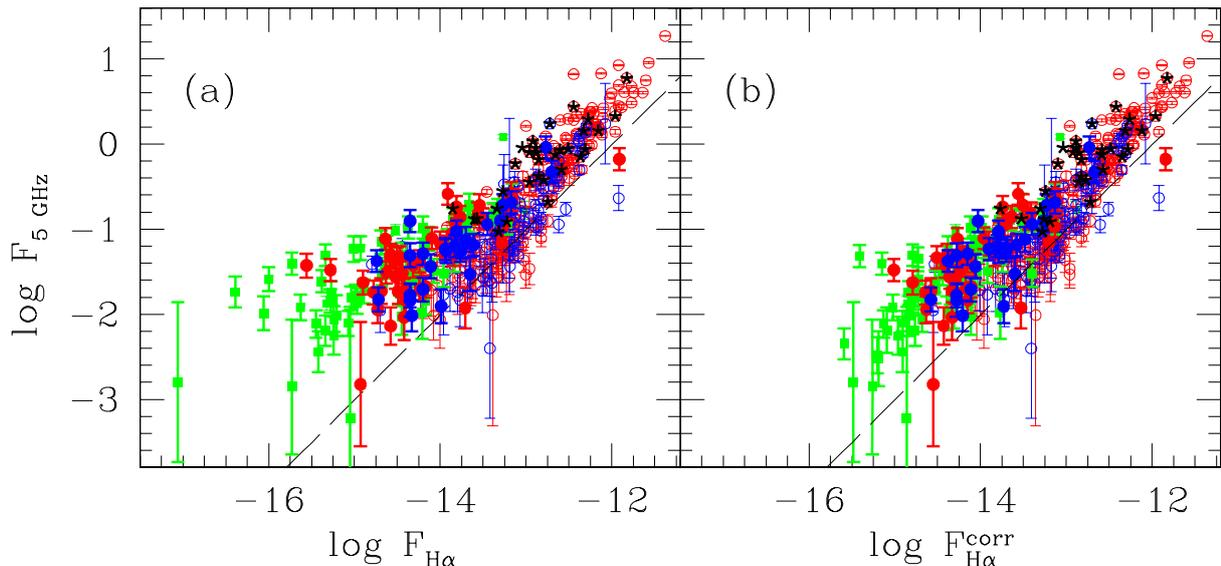


Fig. 3. The $H\alpha$ fluxes in $\text{erg cm}^{-2} \text{s}^{-1}$ measured through aperture photometry at the location of radio sources associated with MIR emission are shown in panel (a) as a function of the radio flux recovered from catalogued data at 5 GHz in mJy. Color coding is the same as in Figure 1 but open symbols have been used. In the right panel (b) we display for the same sources the $H\alpha$ flux corrected for internal extinction. Filled symbols indicates radio fluxes from aperture photometry at 6.3 GHz of b- and c-type MIR sources with no catalogued radio counterpart. The predicted $H\alpha$ emission if the radio flux were due to free-free radiation only is shown with a dashed line. The star symbols indicate the presence of identified SNR in the regions (catalogue code > 8).

YSCs only occasionally host massive stars. Star forming regions with a large non-thermal to thermal radio flux ratio follow the high surface density knots of gaseous filaments while the others are more coarsely placed around or on the filaments.

In the last panel of Figure 4 we plot again the mean non-thermal fraction in apertures with $R_{ap} = R_s$ (green color). We add to these points the mean non-thermal fraction in the annulus between 1 and 1.5 R_s (blue color) and between 1.5 and 2 R_s (magenta color). We can see, by comparing panel (a1) and (a2), that the excess of non-thermal flux for compact bright sources is close to the peak of the emission (green circles) since the external annuli (in magenta) have lower non-thermal fractions. There is no consistent monotonic trend for variations of non-thermal fractions with distance from the radio emission peaks, and no obvious correlation with the radio spectral index given in the catalogue.

In the two panels of Figure 5 we show the correlations between the thermal and non thermal radio continuum at 5 GHz with the $24 \mu\text{m}$ emission. The linear relations in the log-log plane have slopes of 0.50 and 0.68 for the thermal and non thermal radio emission respectively (by minimizing distances of data points to a straight line). The larger scatter at low luminosities in the non-thermal radio continuum-MIR correlation is likely due to non-continuous injections of fast particles and to stochastic sampling of the upper end of the stellar IMF (Initial Mass Function) which settles in as the cluster mass decreases (Corbelli et al. 2009). Turbulent magnetic field amplification and CR acceleration clearly depend on the presence of shocks related to massive stars and might be enhanced in some low luminosity star forming regions that host massive star outliers. The slope of the relation is similar to what Basu et al. (2017) find sampling IC10 at 6.2 GHz on 55 pc scale. The thermal radio continuum declines more slowly with the YSC MIR luminosity than the non-thermal component does. The MIR sources are not overlap-

ping completely with their radio continuum counterparts and in particular they are larger for bright sources. This implies that the total $H\alpha$ flux corresponding to the MIR source, and hence the thermal radio continuum, might be larger in the whole star forming region what has been used in Figure 5 and which refers to the location of the radio source. An additional diffuse radio thermal component might be present for bright sources which would make the MIR-thermal radio continuum correlation steeper. This can be checked in the future at larger scales using radio maps corrected for short spacing.

In Figure 6 we show the galactocentric radial dependences of the MIR-to-radio continuum and MIR-to-thermal radio continuum and non-thermal-to-thermal radio continuum ratios. The green dashed lines are plotted for reference and indicate the median value of the distributions. The radial slopes in the bottom 2 panels of Figure 6 are similar and driven by the radial decrease of dust abundance, particularly evident beyond 3.5 kpc. Sources with $F_{th}/F_{nth} > 1$ at 5 GHz are 40% of the total number of sources at $R < 3.5$ kpc. This percentage decreases to 25% for $R > 3.5$ kpc. Non-thermal emission therefore increases with galactocentric distance although the electron temperature in HII regions increases as well to power thermal emission. This result is consistent with a decrease in the radio thermal fraction on a larger scale going radially outwards in M33 (Tabatabaei et al. 2007c).

5. Radio emission from molecular clouds

One of the most striking aspects of the radio emission is how it follows the star formation. This is true for both the thermal and non-thermal emission. In Figure 7 we compare the radio emission at 1.4 GHz with the thermal dust emission at $24 \mu\text{m}$ in two kpc-size arm regions, one in the northern side and the other on the southern side.

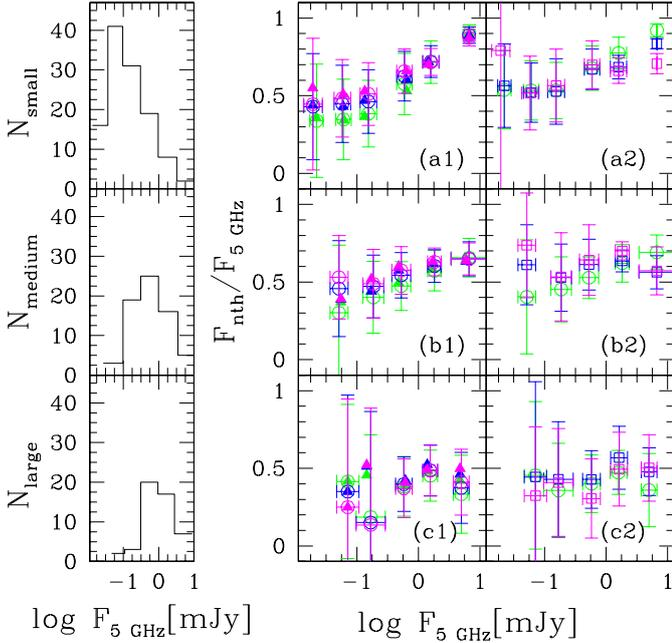


Fig. 4. The non-thermal fraction at 5 GHz of radio sources associated with MIR sources in exposed HII regions is shown in (a1) for small sources, in (b1) for medium sources and in (c1) for large sources as a function of the radio flux density at the same frequency. Filled triangles are the median values, open circles the mean values with the standard deviations. Colors indicates different apertures: green for $R_{ap}=R_s$, blue for $R_{ap}=1.5 R_s$ and magenta for $R_{ap}=2 R_s$. Left panels show the number of sources in each bin for sources of small (top), medium (middle) and large (bottom) size. Right panels display the non-thermal fractions for $R_{ap}=R_s$ (open green circles), in the annulus between R_s and $1.5R_s$ (open blue squares) and between $1.5R_s$ and $2R_s$ (open magenta squares) for small, medium and large sources (a2, b2, c2 respectively). Radio flux units are mJy.

Zooming into 100 pc size regions we can investigate the radio emission from individual molecular clouds and how this relates to other tracers of star formation. Each molecular cloud covers a well-defined region in the sky (e.g. Fig.4 of Corbelli et al. (2017)) and we now discuss the radio emission from the GMC sample, using photometry of the regions within the cloud boundaries. We exclude for the statistical analysis clouds outside the 5 GHz map and in the proximity of NGC604.

We compute both the total radio emission and the residual emission for each GMC. Residual emission has been estimated after subtracting the flux of radio sources in the catalogue of White et al. (2019) associated with each GMC, $F^{GMC} - F^{sracs}$, considering radio sources within the average cloud radius. For individual clouds the residual emission can be negative if, for example, the radio source is close to cloud boundary because some flux might not be within the GMC contour. Table 1 lists for each cloud class the median (F_5^{GMC}) and mean ($\langle F_5^{GMC} \rangle$) fluxes at 5 GHz, the median and mean residual emission ($F_5^{GMC} - F_5^{sracs}$ and $\langle F_5^{GMC} - F_5^{sracs} \rangle$ respectively). In addition we show the mean mass of GMCs, the median and mean H α and 24 μ m fluxes for each cloud class. Radio emission is clearly detected for most of the clouds with exposed star formation (C class) with a wide dispersion: fluxes are distributed mostly between the values of 50 and 5000 μ Jy at 5 GHz with a median value of 282 μ Jy. Radio emis-

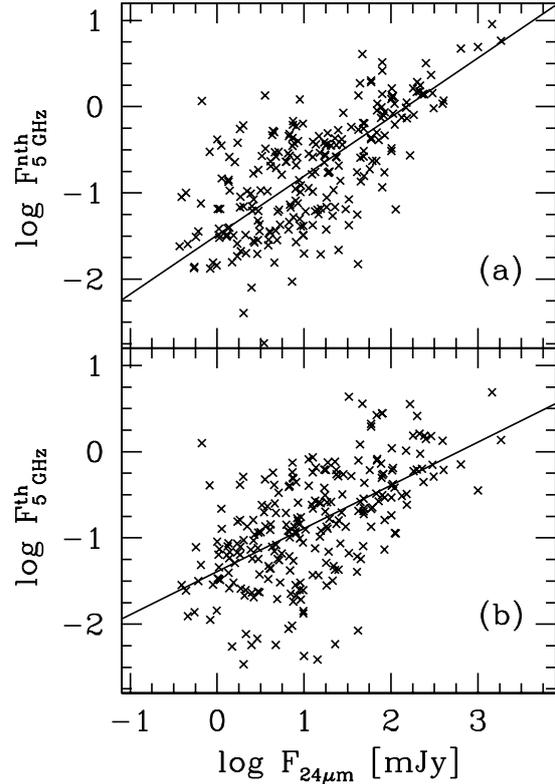


Fig. 5. Correlations between the non thermal (a) and thermal (b) radio continuum at 5 GHz with the 24 μ m emission in 248 exposed HII regions of M33. The lines minimize distances of data points to them and have slopes of 0.68 and 0.50 in panel (a) and (b) respectively. Radio flux units are mJy and have been measured using circular apertures with $R_{ap}=1.5 R_s$.

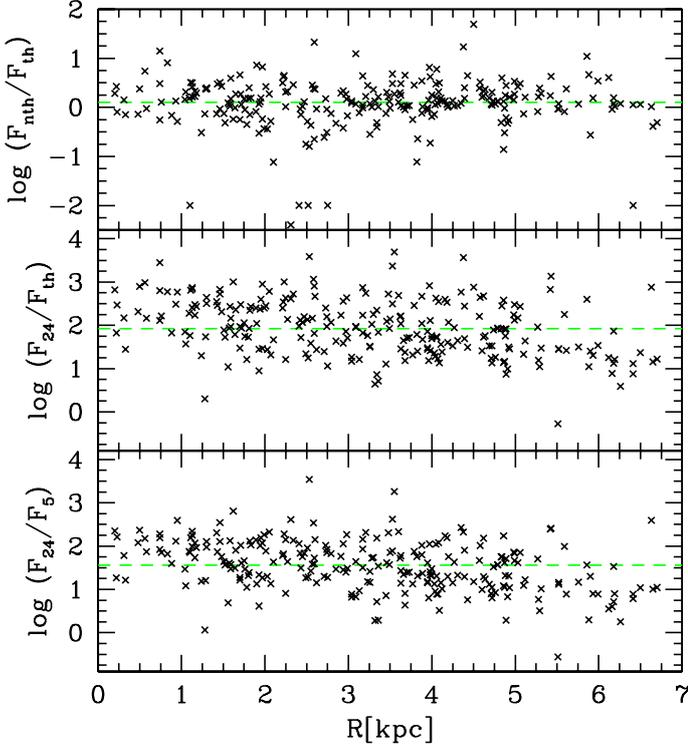
sion at 5 GHz is detected for about 80 % of B-type clouds with most of the fluxes being between 50 and 500 μ Jy and a median value of 20 μ Jy, much lower than for C-type clouds. For inactive clouds, or GMCs without massive star formation (A class), radio fluxes are distributed around the value of zero.

The low detection rate of clouds without star formation is interesting but requires further investigation using radio maps corrected for missing short spacing. Molecular clouds are expected to concentrate magnetic fields, which could result in some diffuse non-thermal emission if cosmic rays penetrate the clouds. There are 3 A-type clouds next to NGC604 which show enhanced radio emission and a double peak in the CO J=1-0 line. Likely strong shocks in the expanding shell of NGC604 compress the surrounding interstellar medium favoring the formation of GMCs and the propagation of relativistic particles streaming along the magnetic field lines. In a future paper, dedicated to the mechanism for cosmic ray acceleration, we will use radio maps corrected for short spacing to examine in more detail diffuse radio emission in GMCs at various stages of evolution and at different locations in the disk.

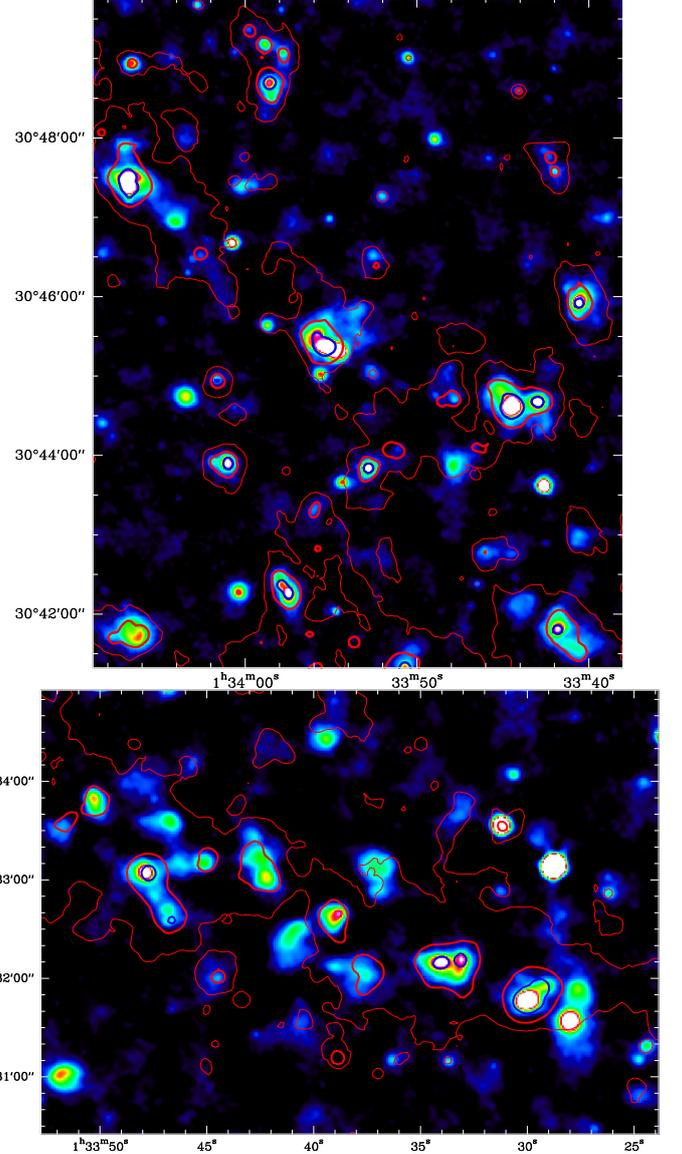
Residual emission, not associated with identified radio sources, is barely present in B-type clouds but it represents about 1/3 of the total radio emission, for GMCs of class C, with

Table 1. Median and mean radio fluxes at 5 GHz, $H\alpha$ and $24\mu\text{m}$ emission for each GMC class

GMC type	GMC N	F_5^{GMC} μJy	$F_5^{GMC-Fsrcs}$ μJy	$F_{H\alpha}^{GMC}$ $\text{ergs cm}^{-2} \text{s}^{-1}$	F_{24}^{GMC} μJy	$iM_{GMC,\zeta}$ M_{\odot}	$iF_5^{GMC,\zeta}$ μJy	$iF_5^{GMC-Fsrcs,\zeta}$ μJy	$iF_{H\alpha}^{GMC,\zeta}$ $\text{ergs cm}^{-2} \text{s}^{-1}$	$iF_{24}^{GMC,\zeta}$ mJy
A	169	-7.	-7.	$7.2 \cdot 10^{-15}$	4.	$1.3 \cdot 10^5$	-2.	-6.	$1.4 \cdot 10^{-14}$	6.
B	86	20.	11.	$1.5 \cdot 10^{-14}$	9.	$2.1 \cdot 10^5$	52.	7.	$2.8 \cdot 10^{-14}$	13.
C	276	282.	85.	$6.7 \cdot 10^{-14}$	19.	$3.6 \cdot 10^5$	795.	251.	$1.5 \cdot 10^{-13}$	48.


Fig. 6. The radial trend of MIR-to-radio flux ratio at 5 GHz (bottom), for the thermal radio emission only (middle), and the non-thermal-to-thermal ratio at 5 GHz (top) are plotted for exposed YSCs with radio counterparts in the catalogue. Dashed green lines are reference lines placed at the median value of the distributions.

exposed star formation. As star formation progresses, and the GMC becomes of C-type with the YSC breaking through the cloud, the increase of radio emission in GMCs is much stronger than any corresponding increase of thermal emission (as indicated by $H\alpha$ recombination lines or hot dust emission). As shown in Table 1, in fact, both $H\alpha$ or $24\mu\text{m}$ emission increase only by a few from B to C class clouds. The average radio emission instead increases by more than one order of magnitude suggesting a substantial increase of the non-thermal component as the YSC evolves. In Figure 8 we show the correlation between the radio and the $H\alpha$ flux from GMCs; in the right panel we have binned the GMCs according to their $H\alpha$ emission. An average correction for extinction has been applied to the $H\alpha$ emission from GMCs using Eq.(8), where all fluxes refer to integrated quantities inside each GMC contour. The trend for the


Fig. 7. We compare radio and MIR emission of a kpc-size region allowing details of tens of parsecs in size to be seen. Color image is 1.4 GHz radio emission from White et al. (2019) shown with a log scale of a portion of the northern (upper panel) and southern (bottom panel) side of M33. Contours are 24 micron Spitzer emission at 1, 3, and 10 (thick blue line) MJy/sr.

red dots, which indicate clouds with exposed star formation (C-type), is very similar to what we found for individual YSCs. The Figure underlines the weaker radio emission of A- and B-type GMCs (magenta and green dots respectively). The large dispersion, as indicated by the errorbars, is due both to variations of the star formation rate in GMCs and to some sidelobe affecting the 5 GHz map.

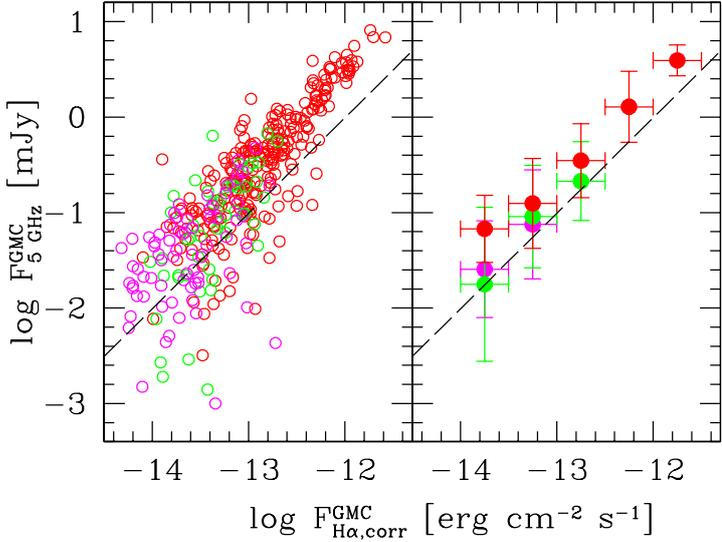


Fig. 8. The radio at 5 GHz versus the $H\alpha$ emission for each GMC is displayed in the left panel. In the right panel the mean radio emission from GMCs in bins of $H\alpha$ is shown. An average correction for extinction, using the $24\ \mu\text{m}$ emission associated with each cloud, has been applied to the $H\alpha$ flux of individual GMCs. Red circles are relative to C-type clouds with exposed YSCs, green circles are for B-type clouds with embedded star formation and magenta circles for inactive clouds of A-type. Only data for GMCs detected at 5 GHz have been used. The dashed line shows the expected thermal component at 5 GHz

6. The link between radio emission and star formation: from GMCs to YSC scale

We have seen in the previous Section that thermal radio emission in HII regions can be estimated from recombination lines such as $H\alpha$ and we have used the $24\ \mu\text{m}$ flux density to correct $H\alpha$ for internal extinction (generally low for exposed YSCs in M33). Extinction corrected $H\alpha$ emission provides an estimate not only of the thermal radio flux density but also of the local star formation rate. For the scales we are examining here, from GMCs to YSCs, star formation is an event that lasts less than the GMC lifetime, the latter being estimated of order 14 Myrs (Corbelli et al. 2017). YSCs start breaking through the cloud when they are about 5 Myrs old, after the embedded phase, (Corbelli et al. 2017). Hence, the timescales involved when sampling GMCs and YSCs are of order 10 Myrs, until the GMC disperses through the ISM. If the stellar mass of the newly formed cluster is not sufficient to fully populate the IMF at its upper end, the $H\alpha$ is no longer a good star formation rate indicator. This affects cluster masses below $10^3 M_\odot$ or $H\alpha$ luminosities lower than $10^{37}\ \text{erg s}^{-1}$, corresponding to a flux of about $10^{-13}\ \text{erg cm}^{-2}\ \text{s}^{-1}$ at the distance of M33 (Sharma et al. 2011). At lower luminosities stochastic sampling of the IMF with occasional formation of massive stars implies one should use mean values of ensembles of sources.

The distribution of the total radio flux at 5 GHz versus the $H\alpha$ flux corrected for extinction, is shown in Figure 9 in a log-

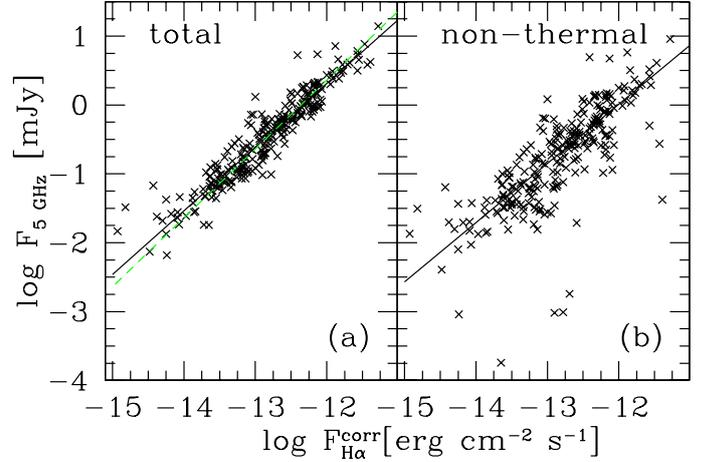


Fig. 9. The total (left panel) and non-thermal radio flux (right panel) at 5 GHz for MIR selected star forming regions plotted as a function of the $H\alpha$ flux corrected for extinction. The relation of the $H\alpha$ emission is tighter with the total radio flux rather than with the non-thermal radio continuum only. The fitted correlations shown are drawn by minimizing distances to the line and their slopes are 0.87 and 0.93 for the total and non-thermal flux respectively. Plotted quantities are relative to circular apertures with $R_{ap}=1.5 R_s$. The green dashed line is the best fitted line with slope unity.

log plot. The straight line, a fit to the data minimizing distances, has a slope 0.93 and a very low dispersion. The dashed green line is the fit to the data if we require a linear relation (a slope of one). The goodness of this fit implies that low mass star forming regions with $H\alpha < 10^{-13}\ \text{erg cm}^{-2}\ \text{s}^{-1}$ or $F_{5\text{GHz}} < 0.3\ \text{mJy}$ are equally dim in radio as in $H\alpha$ emission. The correlation of $H\alpha$ brightness with the non-thermal radio flux density shown by the straight line in Figure 9(b) has a slope of 0.87 and is less tight. This suggests the use of total radio continuum, which does not suffer extinction, as indicator of the SFR. The following equation (Kennicutt & Evans 2012) links the star formation rate with $H\alpha$ luminosities:

$$\frac{SFR_{H\alpha}}{M_\odot\text{yr}^{-1}} = 5.37 \cdot 10^{-42} \frac{L_{H\alpha}}{\text{erg s}^{-1}} = 4.53 \cdot 10^{-4} \frac{F_{H\alpha}}{10^{-12}\text{ergs cm}^{-2}\ \text{s}^{-1}} \quad (10)$$

This is in general an upper limit due to ionizing photon leakage from star forming regions, a problem which affects also the thermal radio continuum. Using the linear relation (green dashed line) shown in Figure 9, we can write

$$\frac{SFR_{5\text{GHz}}}{M_\odot\text{yr}^{-1}} = 1.98 \cdot 10^{-4} \frac{F_{5\text{GHz}}}{\text{mJy}} = 2.35 \cdot 10^{-28} \frac{L_{5\text{GHz}}}{\text{erg s}^{-1}\ \text{Hz}^{-1}} \quad (11)$$

We obtain the same expression when fitting the radio continuum flux density at 5 GHz versus $H\alpha$ emission in GMCs. We can then compare this expression, which applies to discrete events of star formation at small scales, with the SFR integrated over galaxies. Using the FIR-radio continuum correlation to calibrate

the star formation rate in galaxies as a whole (Murphy et al. 2011) this reads:

$$\frac{SFR_{1.4GHz}^{large}}{M_{\odot}yr^{-1}} = 0.64 \cdot 10^{-28} \frac{L_{1.4GHz}^{large}}{erg \ s^{-1} \ Hz} \quad (12)$$

Given the spectral indexes observed for the radio sources (> -0.5) the ratio between YSCs luminosities at 1.4 and at 5 GHz is < 2 . Hence, for a given SFR, equation (12) implies a higher radio continuum luminosity than equation (11). That is to say that the ratio between the $H\alpha$ luminosity and radio continuum luminosity is higher in individual star forming regions than globally, for integrated quantities in spiral galaxies. We recall that we reached a similar conclusion for the ratio between the MIR emission and radio continuum in Section 3, with the exception of a few HII regions. On the other hand it is well known that large scale radio emission in spiral galaxies has a strong non-thermal radio component (Condon & Yin 1990): magnetic fields are pervasive in the ISM and cosmic rays can quickly diffuse away from where they are injected, supporting our finding.

To investigate in more detail the link between the radio emission and the star formation rate, or the ratio of thermal to non-thermal radio continuum flux density, and how these vary from the small to the large scale, we now analyse the sample of GMCs. Cloud complexes generally extend over about 100 pc, occupying a larger area than star forming and HII regions, except for very massive YSCs whose HII regions are very extended and have dispersed their native clouds.

In the left panels of Figure 10 we have added to the YSC data, already displayed in panels (a1)-to-(c1) of Figure 4, the mean GMC non-thermal to total radio continuum ratios. These are computed for each bin of YSC radio continuum flux density considering only molecular clouds associated with the YSCs in that bin. They are shown as a function of the mean radio continuum flux density of the hosted YSCs in each bin. In the middle and top panels, i.e. for small and medium size YSCs, we can see that radio bright YSCs are hosted by GMCs with similar non-thermal to total radio continuum flux ratios. A few bright compact YSCs have higher non-thermal to radio continuum flux ratios than their host GMCs (Fig. 10(a)). This confirms our earlier finding, showed in panels (a2) of Figure 4, that the high non-thermal fractions in these sources decrease when considering a wider area around them. We cannot exclude that the localized excess of non-thermal fractions for a few bright compact radio sources is indeed not correct, but due to an underestimate of the free-free emission which has been considered optically thin (Felli & Panagia 1981; Kobulnicky & Johnson 1999; Johnson et al. 2001).

For extended radio sources, Figure 10(c1) shows that although the associated GMCs follow the same trend with radio flux density as the associated YSCs, they have higher non-thermal fractions, similar to clouds shown in other panels and hosting more compact sources. In this case the HII region is comparable to or larger than the GMC and it is expanding while dispersing the parent cloud. It is conceivable that GMCs associated with some of these sources are leftovers or newly formed, possibly triggered by HII shell expansion.

In the right panels of Figure 10 we plot in red the total-to-thermal radio flux ratio for the whole ensemble of GMCs hosting exposed YSCs (filled red squares). Data has been binned according to cloud star formation rate per unit area and the same data is displayed in all three panels for a direct comparison with the same ratio measured for small (a2), medium (b2), and large (c2) sources (open blue circles). On the x-axis we show the SFR per

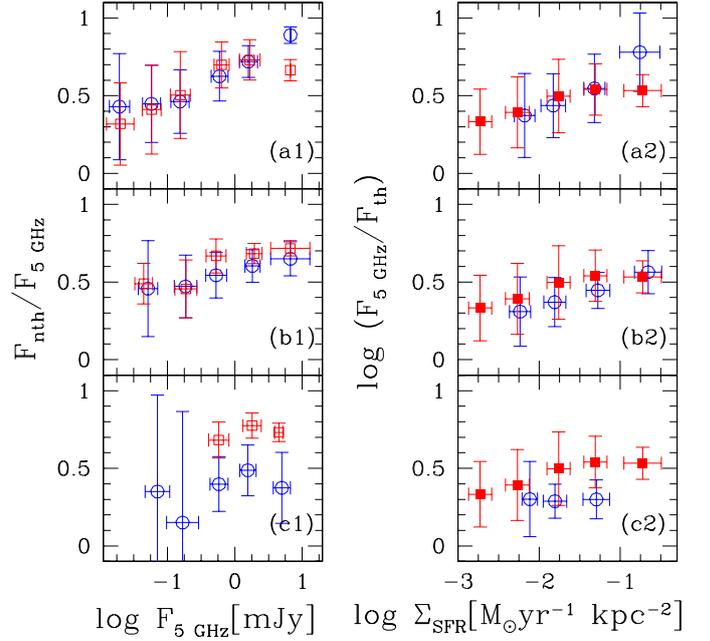


Fig. 10. The left panels show the non-thermal to total radio continuum flux density ratio at 5 GHz in radio sources associated to exposed YSCs (blue circles) using apertures with $R_{ap}=1.5R_s$ for small (a1), medium (b1) and large (c1) sources. In the same panels we show the non-thermal to total radio flux density ratio for GMCs hosting the YSCs (red squares), as a function of the radio emission of the YSCs. Not all YSCs have an associated GMC, especially if they are at large galactocentric radii or spatially very extended. In the right panels we plot the total-to-thermal radio flux ratio for the whole ensemble of GMCs hosting exposed YSCs (filled symbols), binned according to their star formation rate per unit area. Radio continuum has been used to estimate the SFR density (red squares). From top to bottom we compare the GMC ratios with that for the small, medium and large sources respectively (open blue circles) binned according to their SFR per unit area. The area around the source is circular with a radius $1.5 R_s$.

unit area, as traced by radio emission, computed inside cloud contours for GMCs, and in a circular area with radius $1.5R_s$ for YSCs. On the y-axis we display the log of total-to-thermal flux ratio for a direct comparison with the model discussed by Schleicher & Beck (2016) (see their Figure 10). For discrete star forming sites, such as those we are considering here, the Figure confirms that the total-to-thermal radio flux ratio increases with star formation density for compact YSCs and clouds, but there is a flattening for clouds with $\Sigma_{SFR} > 0.03 M_{\odot} yr^{-1} kpc^{-2}$. The extended sources show a remarkably constant ratio of F_{5GHz}/F_{th} of order 2 i.e. there is an equal share between the thermal and non-thermal flux density. The model of Schleicher & Beck (2016) on a larger scale and for a continuous star formation predicts an increase of F/F_{th} with Σ_{SFR} faster than what we observe for compact star forming regions or GMCs. The increasing trend is explained as due to turbulent magnetic field amplification by star formation. But, as the authors point out, discrete injection events cannot maintain a correlation between star formation rate and magnetic field strength. As a consequence, and given also the higher frequency we are sampling, the slower increase of the total-to-thermal radio flux ratio with star formation in our data is

understandable. This relation is lost if we trace the SFR density using $H\alpha$ emission. This underlines the presence of fluctuations in the strength of radiative processes in individual YSCs, due to stochastic events of massive star formation.

6.1. Cosmic ray diffusion and the YSC contribution to non-thermal emission of M33

At scales <1 kpc, Tabatabaei et al. (2013a) conclude that a turbulent magnetic field of order $8 \mu\text{G}$ dominates over the ordered component in M33, and this tangled field implies that cosmic rays during their lifetime diffuse over a relatively short path-length, <400 pc. The CRs are expected to be transported via streaming instabilities at the Alfvén speed $V_A = B/\sqrt{4\pi\rho_{\text{gas}}}$. The average gas volume density in the giant cloud complexes we are considering is of order $10^{-23} \text{ gr cm}^{-3}$ although individual molecular clouds in them, where stars form, have higher densities. For the duration of the star formation phase in GMCs, of order 10 Mys, the CRs can then diffuse over 70 pc, comparable to GMC sizes. Bright and compact YSCs, which have not yet aged, are producing massive stars with discrete injection of CRs: these lag in the surrounding cloud increasing the non-thermal fraction of the cloud radio emission. For extended HII regions, no longer surrounded by molecular gas, the gas density is lower and locally produced CRs, diffuse out quickly. As injections of CRs stop local the non-thermal excess decays.

What is the fraction of the global non-thermal emission of M33 that is in discrete sources such as YSCs or SNRs? Tabatabaei et al. (2007c) have measured the total radio emission of M33 at 6.2 cm and find that the total flux is 1.28 Jy. The total $H\alpha$ flux of M33, corrected for extinction, is about $5 \cdot 10^{-10} \text{ erg s}^{-1} \text{ cm}^{-2}$ (Verley et al. 2009), which implies that on average 1/3 of the emission of M33 at 6 GHz is thermal. For a non-thermal spectral index of -0.8 (Tabatabaei et al. 2007b), the total non-thermal emission at 5 GHz is about 1 Jy. Supernovae in the radio catalogue of White et al. (2019) contribute about 8% to the total non-thermal flux, at 5 GHz, while twice as much, about 16%, is localized around YSCs hosting no known SNRs. We conclude that about 1/4 of the total non-thermal emission at 5 GHz in M33 is linked to discrete current injection events of CRs connected with massive stars evolution. Diffusion of CRs into the ISM from ongoing and past generation of massive stars must account for the remaining fraction.

The mean global star formation density in M33 is $0.0032 M_{\odot} \text{ yr}^{-1} \text{ kpc}^{-2}$, and the ratio of total to thermal flux is 5.7 at 1.4 GHz (Tabatabaei et al. 2007b). This estimate is in very good agreement with that predicted by Schleicher & Beck (2016) model for a continuous star formation law.

7. Summary

The formation of stars can be traced using UV stellar continuum, gas recombination lines such as $H\alpha$ or radio thermal and non-thermal continuum, but also mid-infrared emission of hot dust grains which absorb radiation of the newly formed stars. Star forming galaxies show a tight linear relation between their IR emission and radio continuum luminosities. High angular resolution surveys of the whole star forming disk of the closest galaxies allow today to investigate such relations in individual molecular clouds as the formation of YSCs proceeds, and down to spatial scales below 50 parsecs. In this paper we explore the mid-infrared, radio continuum and $H\alpha$ emission for a large sample of star forming regions in M33 (526 YSCs) and for their na-

tive molecular clouds. The YSCs candidates have been selected for their mid-infrared hot dust emission at $24 \mu\text{m}$ (Sharma et al. 2011). Recent radio surveys of the nearby galaxy M33 have provided a detailed view of the interstellar medium in the radio continuum and a radio source catalogue in the M33 sky area (White et al. 2019). Using this catalogue we find radio continuum source counterparts at 1.4 and 5 GHz for more than half of the MIR sources. We use high sensitivity maps at 6.3 GHz to measure successfully radio emission for the most diffuse and weak ones without a catalogued counterpart.

The radio continuum luminosity of a star forming region establishes a correlation with the $24\mu\text{m}$ luminosity of the associated hot dust component, whose slope is sublinear in the log-log scale. The 24μ luminosity of YSCs fully embedded in the native molecular clouds follows a similar correlation with the radio continuum. We underline that previous attempts to discover embedded star forming sources in M33 through radio continuum selected candidates data have not been successful (Buckalew et al. 2006). Thanks to sensitive radio continuum maps at 6.3 GHz we have been able to confirm, for the first time in a nearby spiral galaxy, the embedded nature of many YSCs associated with molecular clouds with no optical or UV counterparts. Given the variations of the spatial distribution of grains in the HII regions and of the stellar continuum fraction absorbed by dust, it is quite surprising to have found a relation that holds for the overall YSC population, from the embedded to the exposed phase, from the central region to the galaxy outskirts.

The slow chemical enrichment of galaxies with cosmic time and the variety of processes that regulates life cycle and the temperature of dust grains implies that $24 \mu\text{m}$ emission alone might not be sufficient to trace star formation. A combined tracer, IR with UV or hydrogen recombination lines, has become one of the most commonly used star formation rate estimator (Kennicutt et al. 2009). We have shown in this paper that the correlation between the radio continuum at 5 GHz and the combined tracer $24\mu\text{m}$ and $H\alpha$ emission (or extinction corrected $H\alpha$), holds over 4 orders of magnitude at scales between few tens and ~ 100 pcs. The relation is close to linear and extremely tight when data on YSCs refer only to the latest stage of evolution in the host molecular cloud (exposed phase). The correlation is tighter if the total radio continuum is considered rather than the estimated non-thermal radio emission. In examining individual YSCs of low luminosities, stochastic sampling of the IMF at its high mass end increases the dispersion in the relation between hot dust emission and non thermal radio continuum due to stronger variations of turbulent magnetic field amplification and CR production.

We find a significant fraction of the 5 GHz emission being thermal but compact radio bright YSCs have more than half of their radio emission due to non thermal processes. The unambiguous non-thermal emission in star forming regions where the $H\alpha$ flux is greater than $10^{-13} \text{ erg s}^{-1} \text{ cm}^{-2}$, even in the absence of a supernova remnant, implies ubiquitous local production of cosmic rays when the YSC has at least an O7-type star. Indeed theoretical computations predicts that these O-type stars are able to produce a wind and therefore a shock. About 1/4 of the total non-thermal emission of M33 is linked to discrete current injection events of CRs connected with massive stars in YSCs or SNRs. Diffusion of CRs into the ISM from ongoing and past generation of massive stars must account for the remaining fraction.

More extended radio sources, likely associated with evolved HII regions, do not show a correlation between non-thermal fraction and radio luminosity, and have on average lower non-

thermal fractions than more compact ones. We interpret this trend as due to fast diffusion of CRs as the HII shell expands well beyond the native cloud, with CR injections becoming more seldom at a later stage of the cluster evolution. CR diffusion also explain the lower ratios between the radio continuum at 5 GHz and the $24\mu\text{m}$ or $H\alpha$ emission in individual star forming regions of M33 compared to those measured for galaxies as a whole in the local universe.

The radio continuum emission from giant molecular complexes follows a similar correlation with the extinction corrected $H\alpha$ as individual star forming regions. As determined by Corbelli et al. (2017) the duration of the life cycle for M33 molecular clouds is about 14 Gyrs with the mean molecular cloud mass that increases only by a factor 3 going from the initial inactive phase to the embedded one, to the exposed phase prior to cloud dispersal. The radio emission of the whole GMC has a stronger increase as star formation progresses: as the YSC is formed and it starts breaking through the cloud the non-thermal component in the cloud is ubiquitous. Molecular clouds with only embedded sources, or molecular clouds hosting very small YSCs, as well as inactive clouds, have much lower radio continuum luminosities on average: many of them are still undetected in the published surveys.

The non thermal– radio continuum correlation observed for compact YSCs and GMCs with exposed star formation at all galactocentric radii underlines the role of the star-formation induced turbulent magnetic field as the most efficient source of the non thermal radio emission. Tangled magnetic field in turbulent molecular complexes can prevent fast diffusion of cosmic ray electrons to larger scales as suggested by Tabatabaei et al. (2013a). This can be better investigated in the future using adequate deeper radio survey for tracing the diffuse radio emission. We have calibrated the radio continuum emission as star formation tracer at scales of individual star forming regions and GMCs in M33. A shallow increase of the average total to thermal radio flux ratio with the star formation density is measured for compact YSCs as well as for giant molecular complexes. This is in agreement with theoretical models of turbulent magnetic field amplification by star formation, although fluctuations in CR injections during localized star formation events require more specific theoretical modeling. This will shed light on the link between small and large scale radio emission in galaxies.

Acknowledgements. EC acknowledges the support from grant PRIN MIUR 2017 -20173ML3WW01 and from the INAF PRIN-SKA 2017 program 1.05.01.88.04.

References

Aharonian, F., Yang, R., & de Oña Wilhelmi, E. 2019, *Nature Astronomy*, 3, 561
 Appleton, P. N., Fadda, D. T., Marleau, F. R., et al. 2004, *ApJS*, 154, 147
 Basu, A., Roychowdhury, S., Heesen, V., et al. 2017, *MNRAS*, 471, 337
 Bell, E. F. 2003, *ApJ*, 586, 794
 Buckalew, B. A., Koblunicky, H. A., Darnel, J. M., et al. 2006, *ApJS*, 162, 329
 Cesarsky, C. J. & Montmerle, T. 1983, *Space Sci. Rev.*, 36, 173
 Condon, J. J. & Yin, Q. F. 1990, *ApJ*, 357, 97
 Corbelli, E., Braine, J., Bandiera, R., et al. 2017, *A&A*, 601, A146
 Corbelli, E., Braine, J., & Giovanardi, C. 2019, *A&A*, 622, A171
 Corbelli, E., Verley, S., Elmegreen, B. G., & Giovanardi, C. 2009, *A&A*, 495, 479
 Dong, R. & Draine, B. T. 2011, *ApJ*, 727, 35
 Draine, B. T. 2011, *Physics of the Interstellar and Intergalactic Medium*
 Dumas, G., Schinnerer, E., Tabatabaei, F. S., et al. 2011, *AJ*, 141, 41
 Felli, M. & Panagia, N. 1981, *A&A*, 102, 424
 Gordon, S. M., Duric, N., Kirshner, R. P., Goss, W. M., & Viallefond, F. 1999, *ApJS*, 120, 247
 Gratier, P., Braine, J., Rodriguez-Fernandez, N. J., et al. 2012, *A&A*, 542, A108
 Greenawalt, B. E. 1998, PhD thesis, NEW MEXICO STATE UNIVERSITY

Helou, G., Soifer, B. T., & Rowan-Robinson, M. 1985, *ApJ*, 298, L7
 Hoopes, C. G. & Walterbos, R. A. M. 2000, *ApJ*, 541, 597
 Hughes, A., Wong, T., Ekers, R., et al. 2006, *MNRAS*, 370, 363
 Huynh, M. T., Gawiser, E., Marchesini, D., Brammer, G., & Guaita, L. 2010, *ApJ*, 723, 1110
 Johnson, K. E., Koblunicky, H. A., Massey, P., & Conti, P. S. 2001, *ApJ*, 559, 864
 Kennicutt, Robert C., J., Hao, C.-N., Calzetti, D., et al. 2009, *ApJ*, 703, 1672
 Kennicutt, R. C. & Evans, N. J. 2012, *ARA&A*, 50, 531
 Koblunicky, H. A. & Johnson, K. E. 1999, *ApJ*, 527, 154
 Lee, J. H. & Lee, M. G. 2014, *ApJ*, 793, 134
 Long, K. S., Blair, W. P., Winkler, P. F., et al. 2010, *ApJS*, 187, 495
 Magrini, L., Stanghellini, L., Corbelli, E., Galli, D., & Villaver, E. 2010, *A&A*, 512, A63
 Marcolino, W. L. F., Bouret, J. C., Martins, F., et al. 2009, *A&A*, 498, 837
 Muijres, L. E., Vink, J. S., de Koter, A., Müller, P. E., & Langer, N. 2012, *A&A*, 537, A37
 Murphy, E. J., Condon, J. J., Schinnerer, E., et al. 2011, *ApJ*, 737, 67
 Padovani, M., Marcowith, A., Sánchez-Monge, Á., Meng, F., & Schilke, P. 2019, *A&A*, 630, A72
 Parizot, E., Marcowith, A., van der Swaluw, E., Bykov, A. M., & Tatischeff, V. 2004, *A&A*, 424, 747
 Schleicher, D. R. G. & Beck, R. 2013, *A&A*, 556, A142
 Schleicher, D. R. G. & Beck, R. 2016, *A&A*, 593, A77
 Schober, J., Schleicher, D. R. G., & Klessen, R. S. 2016, *ApJ*, 827, 109
 Sharma, S., Corbelli, E., Giovanardi, C., Hunt, L. K., & Palla, F. 2011, *A&A*, 534, A96
 Tabatabaei, F. S., Beck, R., Krause, M., et al. 2007a, *A&A*, 466, 509
 Tabatabaei, F. S., Beck, R., Krügel, E., et al. 2007b, *A&A*, 475, 133
 Tabatabaei, F. S., Berkhuijsen, E. M., Frick, P., Beck, R., & Schinnerer, E. 2013a, *A&A*, 557, A129
 Tabatabaei, F. S., Krause, M., & Beck, R. 2007c, *A&A*, 472, 785
 Tabatabaei, F. S., Krause, M., Fletcher, A., & Beck, R. 2008, *A&A*, 490, 1005
 Tabatabaei, F. S., Schinnerer, E., Murphy, E. J., et al. 2013b, *A&A*, 552, A19
 Verley, S., Corbelli, E., Giovanardi, C., & Hunt, L. K. 2009, *A&A*, 493, 453
 Verley, S., Hunt, L. K., Corbelli, E., & Giovanardi, C. 2007, *A&A*, 476, 1161
 Vink, J. S., de Koter, A., & Lamers, H. J. G. L. M. 2000, *A&A*, 362, 295
 White, R. L., Long, K. S., Becker, R. H., et al. 2019, *ApJS*, 241, 37